Journal Pre-proof

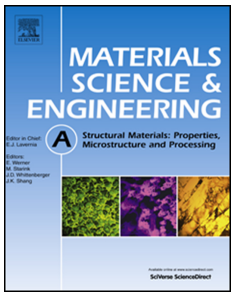

Achieving excellent strength-ductility combination through the control of intricate substructures in an additively manufactured Co–Cr–Mo alloy

Wenting Jiang, Xinglong An, Song Ni, Li Wang, Junyang He, Zibin Chen, Yi Huang, Min Song

PII: S0921-5093(23)01111-5

DOI: https://doi.org/10.1016/j.msea.2023.145687

Reference: MSA 145687

To appear in: *Materials Science & Engineering A*

Received Date: 3 August 2023

Revised Date: 31 August 2023

Accepted Date: 12 September 2023

Please cite this article as: W. Jiang, X. An, S. Ni, L. Wang, J. He, Z. Chen, Y. Huang, M. Song, Achieving excellent strength-ductility combination through the control of intricate substructures in an additively manufactured Co–Cr–Mo alloy, *Materials Science & Engineering A* (2023), doi: https://doi.org/10.1016/j.msea.2023.145687.

Achieving excellent strength-ductility combination through the control of intricate substructures in an additively manufactured Co-Cr-Mo alloy

Wenting Jiang [a], Xinglong An [a], Song Ni [a,*], Li Wang [a], Junyang He [a,*], Zibin Chen [b], Yi Huang [c,d], Min Song [a]

a -State Key Laboratory of Powder Metallurgy, Central South University, Changsha 410083, China

b - Research Institute for Advanced Manufacturing, Department of Industrial and Systems Engineering, The Hong Kong Polytechnic University, Hong Kong, China

c - Department of Design and Engineering, Faculty of Science and Technology, Bournemouth University, Poole, Dorset BH12 5BB, UK

d - Materials Research Group, Department of Mechanical Engineering, University of Southampton, Southampton SO17 1BJ, UK

Abstract

In this study, we successfully endowed a classical Co25Cr5Mo5W alloy with excellent strength-ductility combination by regulating the substructures during laser powder bed fusion (LPBF) and subsequent heat treatment. State-of-the-art characterizations reveal that the as-built Co25Cr5Mo5W alloy features integrated networks of dense cell boundaries and stacking faults within a pure face-centered cubic matrix, which jointly confer a high yield strength of ~820 MPa and a high ductility of ~22.3%. Upon heat treatment, the heavy decoration of solutes Cr, Mo, W, and Si at cell boundaries triggers heterogeneous nucleation and growth of Laves precipitates within 15 minutes. After that, global intercellular precipitation occurs, further boosting the yield strength to ~1170 MPa at a decent ductility of ~7.5 % when heat-treated for 60 minutes. Such a finding establishes a clear connection between the substructures and the mechanical properties, offering valuable implications for surpassing the current mechanical limitation in the Co-Cr-Mo alloy family.

Keywords: Additive manufacturing; Cobalt-chromium-molybdenum alloy; Stacking fault; Precipitation behavior; Mechanical properties

*Corresponding authors. Email: song.ni@csu.edu.cn; junyanghe@csu.edu.cn

1. Introduction

Cobalt-chromium-molybdenum (CCM) alloys have found extensive application in the fields of dentistry and orthopedics, such as dental crowns and knee replacements. This widespread use can be attributed to their superior integrated properties, encompassing strength, wear resistance, corrosion resistance, and biocompatibility [1-3]. CCM alloys typically exhibit a dual-phase structure consisting of a hexagonal close-packed phase (ε-HCP phase), which represents a hard and brittle martensitic transformation product [4], and a face-centered cubic phase (γ-FCC phase) that serves as the soft matrix [5]. In this wise, regulating the formation of the two phases, specifically in terms of volume fraction and morphology, is key for achieving optimal mechanical properties [6]. In the as-cast state, CCM alloys often exhibit an excessive fraction of ε phase as a result of a low cooling rate [7]. To address this issue, post-heat treatment or alloying is required to increase the fraction of the γ phase. However, while the thermomechanical route is often complex and energy-consuming, e.g., uniaxial hot compression used in [8], the available alloying (e.g., N) across the periodic table is rather limited considering elemental biotoxicity [9, 10]. In light of these concerns, additive manufacturing (AM) presents a viable alternative for the production of CMM alloys with high fraction of γ phase. The ultrahigh cooling rate of up to 10^5-10^6 K/s associated with AM helps suppress the dynamics of martensitic transformation [9, 11, 12]. For instance, Kajima et al. [13] successfully prepared a pure γ phase CMM alloy using LPBF, although the resulting yield strength-ductility combination (837 MPa-12.3 %) was not particularly impressive. Similarly, in another LPBF fabricated Co-Cr-Mo-W alloy, the overall ductility dramatically improved compared to the as-cast counterpart (24.5 % vs. 3.4 %) due to a substantial reduction in the ε fraction [7]. Besides, LPBF specimens often bear high residual stress inherited from the rapid heating-cooling history [3, 14, 15], which detrimentally affect mechanical properties and influence the stress-induced martensitic transition (SIMT) behavior in CCM alloys [16, 17].

Secondary precipitates have also been introduced to improve the mechanical performances of CCM alloys, including intermetallic compounds, carbides and nitrides [18-20]. Unfortunately, these precipitates are inherently brittle and tend to coarsen rapidly along internal interfaces, such as grain boundaries. The heterogeneous configuration of these interfaces leads to the heterogeneous distribution of the precipitates, rendering a poor balance between strength and ductility [21, 22]. Recent studies have focused on modulating the precipitation process by alloying and thermomechanical processing, but the effect is still far from satisfactory [23, 24]. In light of an essential microstructural feature induced by AM,

namely nano-sized cells serving as dense and near-homogeneous precipitation nucleation sites, we may realize a better precipitation control in these CCM alloys. For example, Ye et al. conducted heat treatment on an AM-ed Co30Cr6Mo alloy and observed the fine dispersion of particles within the matrix, resulting in remarkable comprehensive mechanical properties compared to the as-cast counterpart[25]. However, controversy still exists on whether the precipitation process can be truly optimized. For example, Santecchia et al. found that the heat treatment of an LPBF Co-Cr-Mo-W alloy results in the fast coarsening and elongating of the precipitates, significantly impairing ductility performance [26, 27].

Based on the aforementioned observations, it can be inferred that the reported mechanical performance of AM-produced CCM alloys varies from case to case, suggesting that the application of AM technology to the CMM alloy family is still in its early stage. Possible reasons for this include: (1) the insufficient integration of the unique cell substructure induced by the LPBF process and the extremely low stacking fault energy (SFE) of CCM alloys in alloy design. (2) the lack of comprehensive understanding and exploitation of the relationship between LPBF microstructural features and subsequent precipitation, resulting in elusive control over precipitation behavior for improved mechanical performance.

To tackle these concerns, this study focuses on the fabrication of a Co25Cr5Mo5W (wt. %) alloy (referred to as ISO 5832) using LPBF, followed by various heat treatment processes. The LPBF Co25Cr5Mo5W alloy exhibits a typical cell substructure associated with dense stacking fault (SF) networks, resulting in excellent tensile strength-ductility combination. We conducted a detailed investigation of the precipitation behavior at 900 °C, spanning nucleation to coarsening, and successfully correlated it with the evolution of mechanical properties. The findings from this work will provide valuable insights for overcoming the current mechanical limitations in the CCM alloy family by leveraging the capabilities of AM technology.

2. Material and methods

2.1 Specimen preparation

A Co25Cr5Mo5W (wt.%) alloy was prepared by LPBF and also by vacuum arc melting for comparison (referred to as the as-cast state). For LPBF, the alloy powder was fabricated by gas atomization in a nitrogen atmosphere and the powder was of spherical shape with a diameter size range of 35-55 μm, as shown in Fig.1a. The X-ray diffraction (XRD) pattern taken on the D/max2550pc

machine using Cu Kα radiation indicates a nearly pure γ-FCC phase structure of the alloy powder. The chemical composition measured by Inductively Coupled Plasma (ICP) was (in weight percent, wt.%): 25.56 Cr, 5.01 Mo, 5.68 W, 1.86 Si, 0.7 Mn and Co balance, complying with the ASTM F75 standard. The scanning electron microscopy (SEM) energy dispersive spectrometry (EDS) analysis of a particle shown in Fig.1b confirmed the uniform distribution of the principal elements. The LPBF process was carried out using an FS271 machine (Farsoon, China) protected by argon gas and the oxygen content was less than 0.1%. The parameters of the LPBF process were: laser power of 160 W, hatch spacing of 0.07 mm, scanning speed of 400 mm/s and layer thickness of 0.03 mm. The specimens were printed layer-by-layer on a 50 mm-thick substrate plate of 45# steel, with a total height of ~ 2 mm. Fig. 1c shows the schematic diagram of the laser beam scanning strategy, where the scanning direction in the LPBF process was kept at 67° angle rotation for the two consecutive layers. The LPBF parts were further divided from the substrate plate and then wire-cut into sheets (each with a thickness of ~ 1.5 mm) using electrical discharge machining. For vacuum arc melting, the as-cast alloy ingot was prepared by the repeated melting (5 times) of a mixture of raw materials with purity larger than 99.5%.

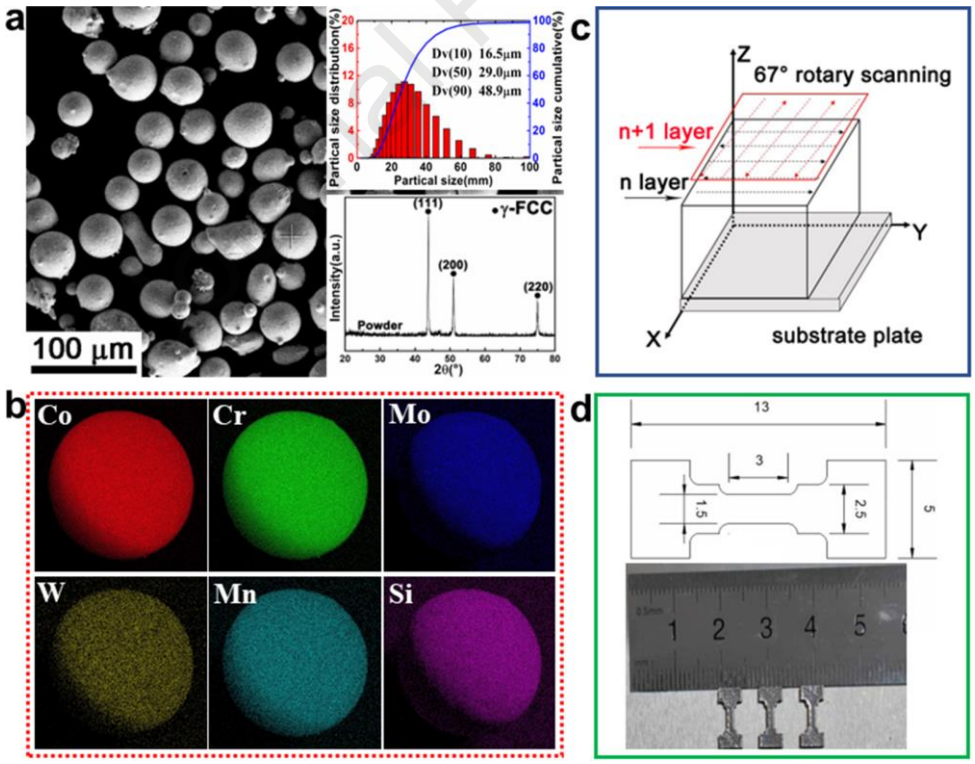

Fig. 1 (a) Morphology, particle size distribution and constituent phase of the powder for LPBF. (b) SEM-EDS analysis of a particle showing the uniform distribution of the principal elements. (c) Schematic diagram of the laser beam scanning strategy. (d) Geometry of the dog-bone shaped tensile testing samples.

2.2 Heat treatment

The LPBF sample were furnace-heated from room temperature to 900 °C at a heating rate of 10 °C /min, followed by different holding durations of 3 mins, 7 mins, 10 mins, 15 mins, 30 mins, 60 mins in the furnace, respectively. After heat treatment, all samples were cooled in air. For the convenience of discussion, we hereafter denote the LBPF specimen without heat treatment as the as-built alloy, and the heat-treated specimens as the HT3, HT7, HT10, HT15, HT30, and HT60 alloys, respectively.

2.3 Mechanical property test

The gauge geometry of the dog-bone shaped tensile specimen was 3 mm (length) and 1.5×2 mm^2 (cross-section) see the picture in Fig. 1d. Tensile tests were performed using an Instron universal testing machine at room temperature, and the strain rate was 2×10^{-3} s^{-1}. The strain was measured using an optical strain gauge (Instron; AVE 2-2663-901). Three specimens at each heat treatment state (including as-built) were tested to guarantee the repeatability of the data. The ultimate tensile strength (UTS), yield strength (YS), and elongation of the tested specimens were obtained from the engineering stress-strain curve.

2.4 Microstructural characterization

Microstructures of all specimens were characterized by optical microscopy (OM), SEM (Model Quanta 250 FEG), electron backscattered diffraction (EBSD; Helios NanoLab G3 UC, FEI Czech Republic) and transmission electron microscopy (TEM; Titan G2 FEI). OM, SEM and EBSD specimens were prepared by sandpaper grinding, fine polished using W2.5, W1.5, W0.5 diamond polishing paste, and mirror polished using 0.02 μm colloidal silica (OP-S). EBSD data were analyzed by the TSL OIM 8.0 software. TEM specimens were prepared by sandpaper grinding to the thickness of 70 μm with water across the entire grinding process, and subsequent twin-jet electro-polished using 7 vol% perchloric acid and 93 vol% alcohol as an electrolyte at the voltage of 30 V and a temperature of -35 °C. TEM data were analyzed by the Volex software. The elemental distributions of alloy specimens were determined using STEM-EDS. Atomic scale compositional analysis was conducted using atom probe tomography (APT; LEAP 5000XR). The volume fraction of precipitates was approximated by the area fraction calculated using the Image Pro Plus (IPP) software.

3. Results

3.1 Mechanical properties and fracture surface

Fig. 2a shows the tensile engineering stress-strain curves of the as-built and heat-treated Co25Cr5Mo5W alloys. Notice a curve from the as-cast counterpart is also included for comparison. Clearly, the as-built alloy exhibits superior ductility (fracture elongation, FE, ~ 22.3% vs. ~ 7.5%) and yield strength (YS) (~ 820 MPa vs. ~ 440 MPa) compared to the as-cast alloy, indicating that AM itself, in absence of any post thermomechanical processes, can effectively improve the mechanical performance. Further heat treatment at 900 °C for 3 mins, 7 mins and 10 mins, however, decreases the elongation quickly without apparent compensation in YS. The YS and FE of the HT7 alloy are ~ 843 MPa and ~ 17.9%, respectively, still much higher than that of the as-cast sample. With continuously increasing the holding time over 15 mins, the strength starts to increase sharply. After heat treatment for 60 mins, the YS and UTS reach as high as ~ 1170 MPa and ~ 1395 MPa, respectively, and the FE remains acceptable at ~ 7.5%. Fig. 2b summarizes the mechanical properties of the current Co25Cr5Mo5W alloy as well as those reported in recent literature[6, 24, 25, 28-30]. The Fig. 2c shows the results of mechanical properties of all specimens. Clearly, our AM-ed alloys outperform other AM-ed and casted (with/without heat treatment) Co25Cr5Mo5W alloys in strength-ductility combination. Figs. 2d1 and d2 show the fracture surfaces of the as-built and HT60 alloys after tensile tests, respectively. As marked by red arrows, dimples prevail in the as-built specimen, indicating a typical ductile fracture mode. Plenty of smooth cleavage steps in the heat-treated sample can be found, as marked by green arrows in Fig. 2d2, evidencing a brittle fracture mode. The fracture behaviors of these alloys agree well with their tensile ductility performances.

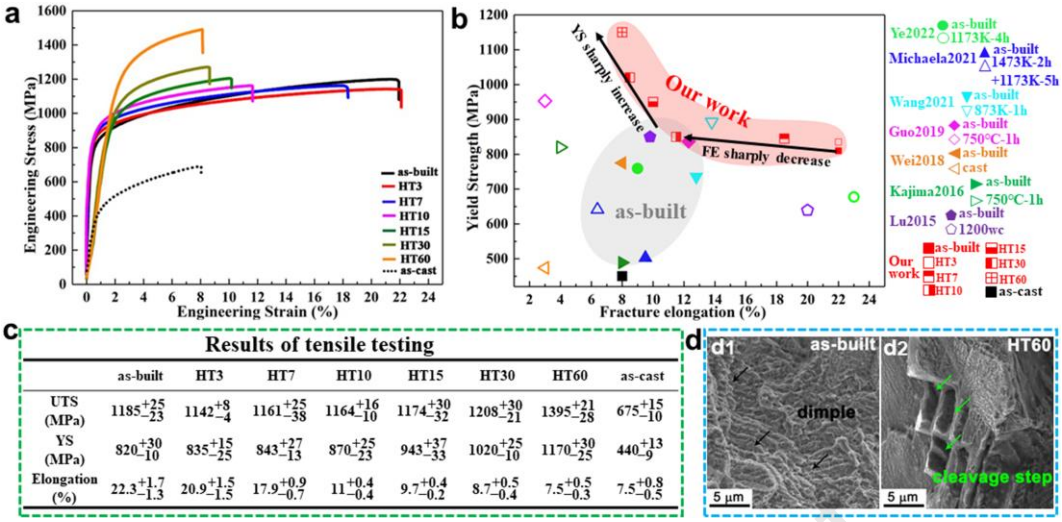

	as-built	HT3	HT7	HT10	HT15	HT30	HT60	as-cast
UTS (MPa)	1185^{+25}_{-23}	1142^{+8}_{-4}	1161^{+25}_{-38}	1164^{+16}_{-10}	1174^{+30}_{-32}	1208^{+30}_{-21}	1395^{+21}_{-28}	675^{+15}_{-10}
YS (MPa)	820^{+30}_{-10}	835^{+15}_{-25}	843^{+27}_{-13}	870^{+25}_{-23}	943^{+37}_{-33}	1020^{+25}_{-10}	1170^{+30}_{-25}	440^{+13}_{-9}
Elongation (%)	$22.3^{+1.7}_{-1.3}$	$20.9^{+1.5}_{-1.5}$	$17.9^{+0.9}_{-0.7}$	$11^{+0.4}_{-0.4}$	$9.7^{+0.4}_{-0.2}$	$8.7^{+0.5}_{-0.4}$	$7.5^{+0.5}_{-0.3}$	$7.5^{+0.8}_{-0.5}$

Fig. 2 (a) Tensile engineering stress-strain curves of the as-built, heat-treated and as-cast Co25Cr5Mo5W alloys. (b) Comparison of the mechanical properties of the current Co25Cr5Mo5W alloys with those reported in the literatures. (c) Collection of tensile property indexes. (d) Typical fracture surfaces of the as-built (d1) and the HT60 (d2) samples.

3.2 Microstructures of the as-built alloy

Fig. 3a and b are the EBSD inverse pole figure and phase map, respectively, showing the microstructure on the longitudinal section of the as-built sample. We observe that the grain sizes fall in the range of 50-80 μm while γ phase (in red) dominates the as-built phase structure, with very few ε phase (in green) discretely embedded, which is consistent with the results of high magnification EBSD (supplementary Fig. S1a) and XRD (supplementary Fig. S2) measurements. The pole figures of the as-built sample are shown in Fig. 3c. For structural details, Fig. 3d presents a high magnification SEM image of the as-built alloy, where nano-sized close-packed cell substructures are clearly seen. The average cell size is measured as 0.95 μm. Fig. 3e then presents a low magnification electron channeling contrast (ECC) image of the as-built alloy and the magnified image of the area marked with a red square box is given in Fig. 3f. Interestingly besides those cells, dense distributions of multi-directional thin planar defects are observed, forming networks throughout the as-built microstructure. These planar defects are identified as SFs and SF bundles from a TEM-based high-resolution image shown in Fig. 3g, which is a sign of a low stacking fault energy (SFE) . These observations together suggest that the SF network interacts with the cells, together constructing a complex three-dimensional (3D) defects configuration within the simple FCC matrix.

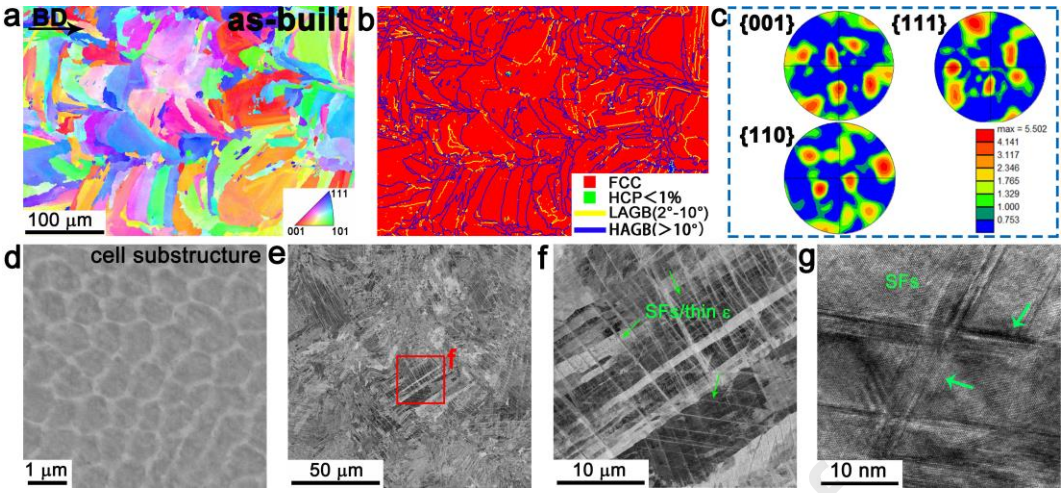

Fig. 3 Observations of the typical microstructures of the as-built alloy. (a) EBSD IPF map, (b) phase and boundary map, and (c) pole figures of the as-built alloy. (d) SEM image showing the configuration of the cell substructures. (e,f) ECC images showing dense distributions of multi-directional thin planar defects. (g) High-resolution TEM image showing the SFs and SF bundles.

Here, with the help of the state-of-the-art APT technology, we manage to precisely portray the elemental distribution at the near-atomic scale in the as-built sample. The tip sample is taken from the red rectangle region as shown in Fig. 4a, with a magnified HAADF image focusing on a cell boundary (CB) given in Fig. 4b. Notice that the CB presents as a bright thin film having tens of nanometers in width. The corresponding STEM-EDS images are demonstrated in Fig. 4c, revealing that the element segregation at the CB is so slight that the results of STEM-EDS are inconspicuous. The 3D semi-transparent atomic distribution maps of Co, Cr, Mo, W, Si, Mn and O are shown in Fig. 4d. We readily observe a band-like Cr, Mo, W, Si-rich region (dashed pink box) cutting across the tip volume. The band region has a width of 30-40 nm, which is very similar to the thin CB film in Fig. 4b. In this light, we propose that the formation of such a segregation-affected band-like zone in the CB vicinity is associated with the change of dislocation configuration into cells during LPBF. Besides, a 30 nm particle enriched in Mo, W and Si, a 10 nm particle enriched in O and Mn, and a planar feature slightly poor in Co and Si are also identified, likely being the preexist precipitates, oxides, and SFs. A closer view of the CB is plotted by the iso-surfaces of W (dark purple), Si (grey) and O (blue) in Fig. 4e at threshold values of 2.7%, 5.2% and 3.8%, respectively. The dashed pink box again outlines the segregation-affected zone along CB. Fig. 4f shows the composition profiles along lines 1, 2 and 3 in Figs. 4d and e. We can then quantify the composition at the segregated CB (Mo 6.0 at. %, W 2.3 at. %, Si 3.6 at. %), the large

precipitate (Mo 12.1 at. %, W 3.7 at. %, Si 6.2 at. %), the small oxide particle (Mn 0.5 at. %) and also the planar defect (Mo 3.0 at. %, W 1.75 at. %, Si 1.5 at. % Mn 0.75 at. %). It is seen that while the elemental decoration along SFs is extremely weak, the CBs attract numbers of Mo, W and Si atoms that similarly (yet to a less extent) constitute the precipitate.

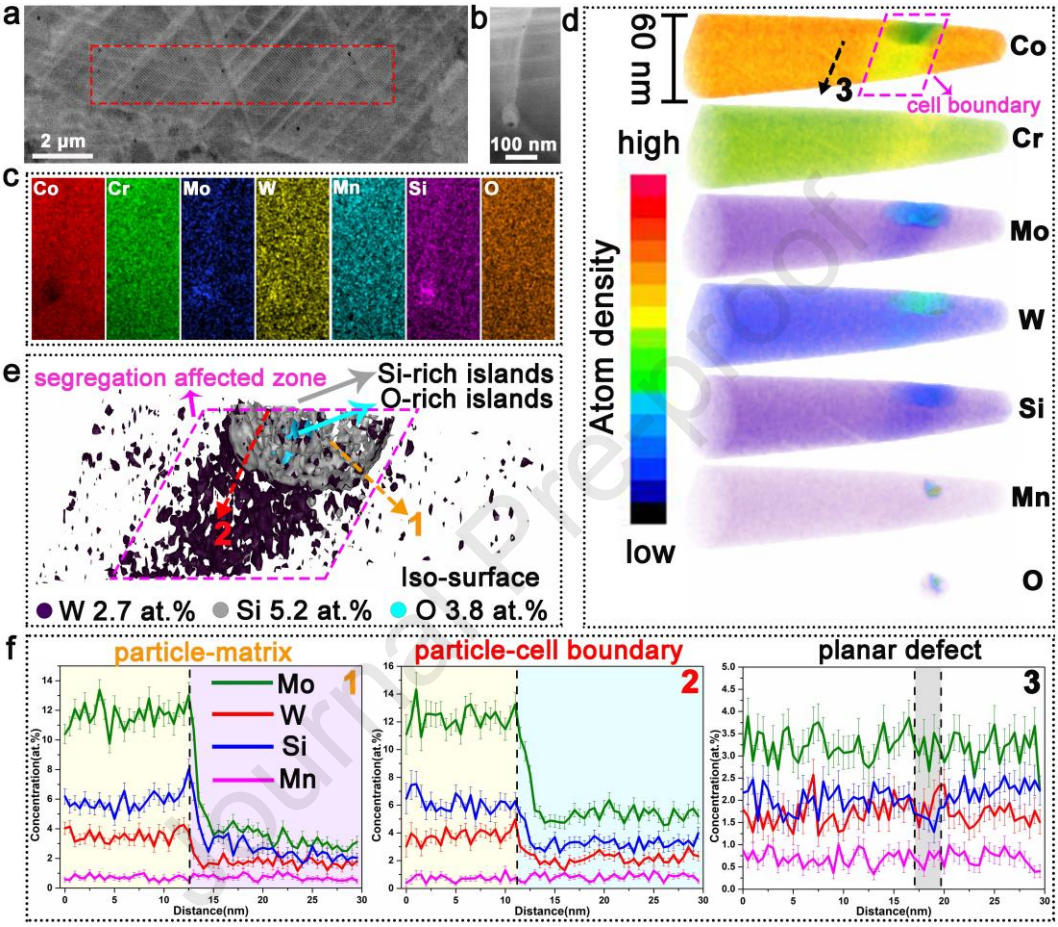

Fig. 4 (a) ECC image showing the region where the tip APT sample is taken. (b) Magnified HAADF image focusing on a cell boundary and (c) the corresponding STEM-EDS maps. (d) 3D semi-transparent atomic distribution maps of Co, Cr, Mo, W, Si, Mn and O. (e) Closer view on the cell boundary region outlined by the iso-surfaces of W, Si and O. (f) Compositional profiles along lines 1, 2 and 3 in (c) and (d).

In contrast, the as-cast counterpart is composed of the major ε phase and the minor γ phase with micron-scale precipitates embedded, see Supplementary Fig. S3. The brittle ε matrix as well as the coarse precipitates are hence believed responsible for the degraded mechanical performance of the same CCM alloy at the as-cast state, also see the literature [7]. To avoid repetition, we will not involve further

discussion on the as-cast counterpart in the following.

3.3 Microstructures of the heat-treated alloys

Fig. 5 shows the microstructures of the HT60 Co25Cr5Mo5W alloy. The EBSD analysis results are given in Figs. 5a-c. Similar to the as-built state, the phase structure at the heat-treated state is again dominated by the γ phase with the ε phase volume fraction < 1%, which is consistent with the results of high magnification EBSD (Fig. S1b) and XRD (Fig. S2). Besides, the crystallographic orientation and grain sizes remain nearly the same (40 μm and 35 μm for the as-built and HT60, respectively), suggesting a decent overall thermal stability of the as-built microstructure against heat exposure at such a high temperature. The pole figures of the HT60 sample are shown in Fig. 5c. The ECC images in Figs. 5d and 6e show the microstructural details of the HT60 alloy. Although the phase constitution does not change, numerous precipitates at around 100 nm in diameter are densely formed throughout the sample. Figs. 5f to 5g are TEM and high-angle annular dark field-scanning transmission electron microscopy (HADDF-STEM) images concentrating on these precipitates, presenting in either short rod-like or ellipsoid morphology without clear orientation preference. The EDS mapping confirms that these precipitates are rich in Mo, W and Si, the same as the preexist precipitates probed by APT. Moreover, dense SF networks can still be clearly distinguished, but not for cells. This is likely due to the overlapping of the coarse precipitates to the cell boundaries.

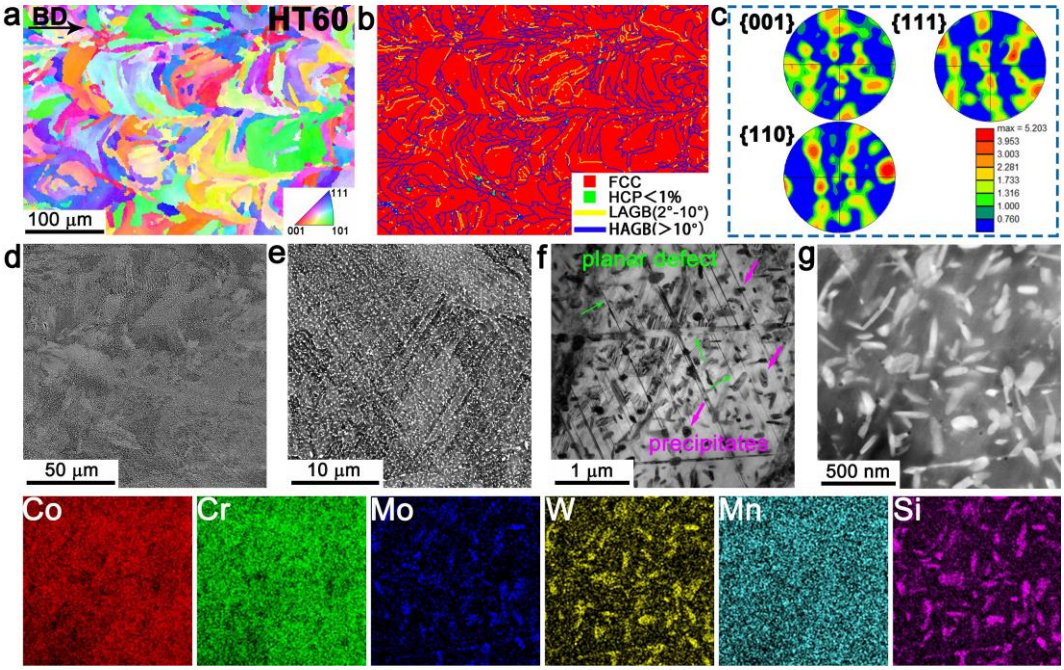

Fig. 5 Observations of typical microstructures of the HT60 alloy. (a) The EBSD IPF map, (b) phase and boundary maps, and (c) pole figures of the HT60 alloy. (d)(e) ECC images showing numerous precipitates throughout the sample. (f) TEM BF image of the HT60 alloy. (g) HADDF-STEM image and corresponding EDS mappings, showing that the precipitates are rich in Mo, W, and Si.

Actually the above precipitates are of the same crystalline structure despite their morphology differences, with an example given in the following Fig. 6. Fig. 6a is an HAADF image concentrating on one precipitate while Fig. 6b is a high-resolution HAADF image taken from the matrix/precipitate interface, showing the difference in atomic stacking sequence between the matrix and the precipitate. According to the fast Fourier transformation (FFT) images in Figs. 6c and 6d, the precipitate has an hcp-type Laves structure, holding a $< 1\bar{2}1\bar{3} >$p//<110>γ orientation relationship to the γ-FCC matrix. Corresponding STEM-EDS mappings are given below and the chemistry details are measured and summarized in Table 1. Based on both the XRD results in supplementary Fig. S2 and the TEM characterization in Fig. 6 by measuring the lattice spacing values, these precipitates can be then determined as the $Co_3(Mo,W)_2Si$ Laves phase [31, 32].

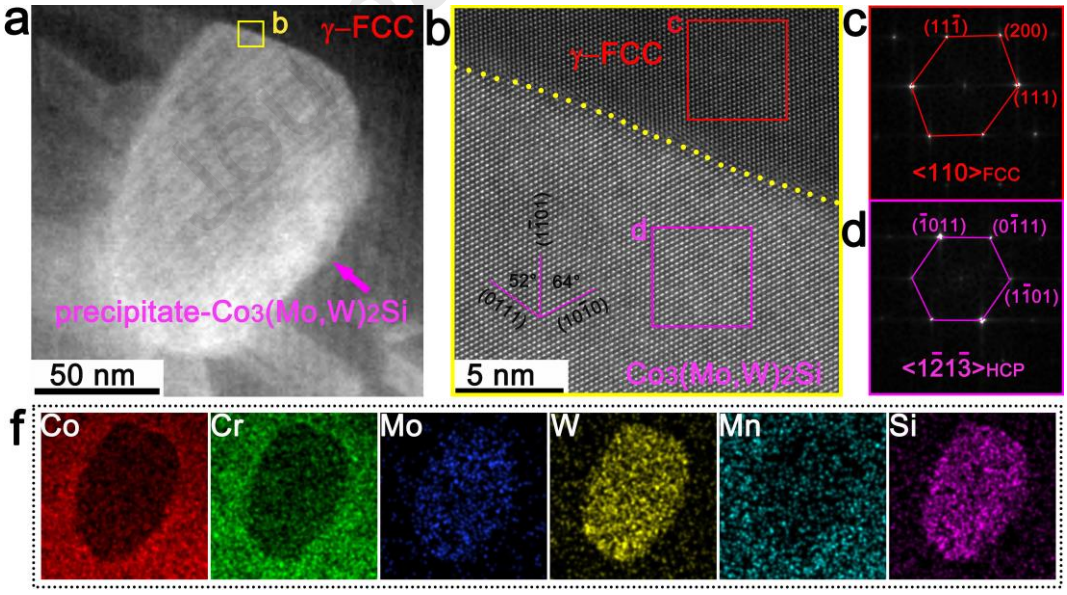

Fig. 6 (a) HAADF image showing the morphology of a randomly selected precipitate. (b) High-resolution HAADF image taken from the matrix/precipitate interface, showing the difference in atomic stacking sequence between the matrix and the precipitate. (c,d) FFT images of the matrix and precipitate in (b). (f) STEM-EDS mappings showing the chemistry details of the area in (a).

Table 1 Chemical compositions of different phases in the as-built and HT60 alloys measured by TEM-EDX (at. %)

Alloys	Phases	Chemical compositions (at. %)					
		Co	Cr	Mo	W	Mn	Si
as-built	matrix	63.3	29.7	2.2	1.6	0.9	2.3
HT60	matrix	63.0	30.7	1.9	1.3	1.0	2.1
	precipitate	40.8	17.7	17.0	9.3	0.2	15.0

3.4 Microstructures after deformation

Figs. 7a-d are the EBSD phase maps and ECC images showing the deformed microstructures of the as-built and HT60 alloys. As shown in Fig. 7a, a large fraction of ε laths, ~ 49%, are observed, indicating the vast occurrence of γ → ε martensite phase transformation during tensile deformation. The ECC image in Fig. 7b further evidences the presence of multi-directional ε phase with a width even down to tens of nanometers. As shown in Fig. 7c, such deformation induced γ → ε transformation also prevails in the HT60 alloy, yet the total fraction of ε phase, ~ 22%, is much less than that in the deformed as-built sample at the similar area near fracture. According to the ECC image in Fig. 7d, the huge difference in martensitic transformation behavior seems well-related to the existence of the dense Laves precipitates. It is likely that the nucleation of the martensitic transformation is promoted by providing extra nucleation sites at the Laves phase boundaries, while the growth and thickening of the martensite laths are, on the contrary, greatly restricted by the pining of the Laves precipitates [19, 31]. More details will be discussed in the following section.

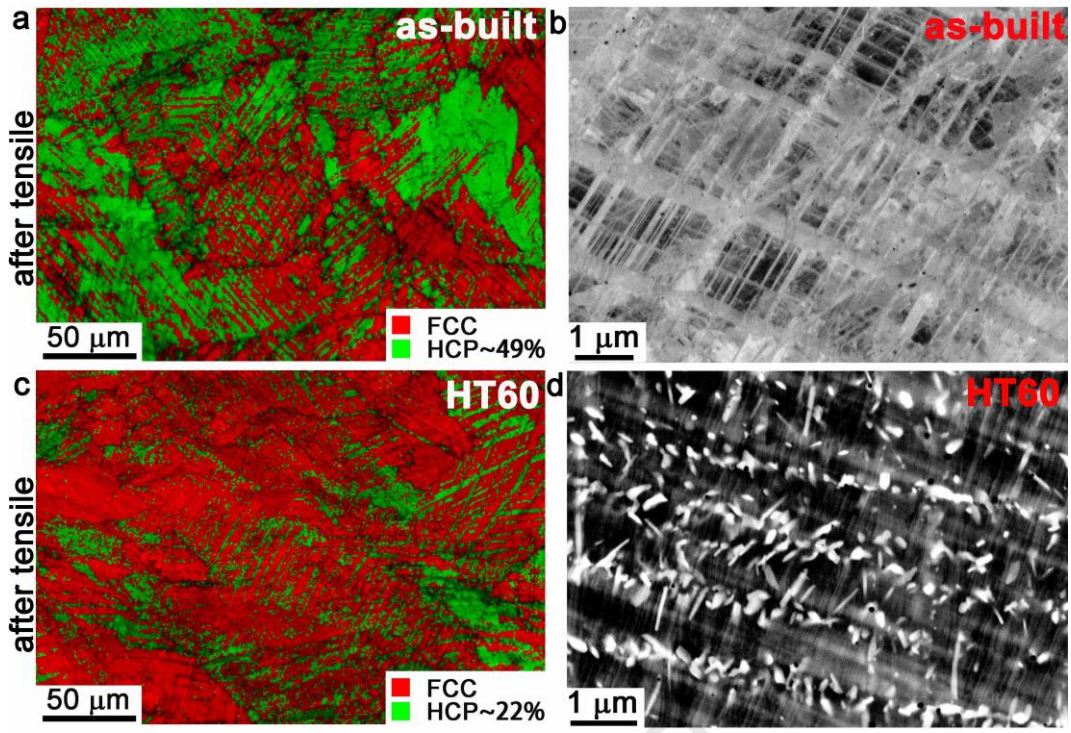

Fig. 7 Deformed microstructures of the as-built and HT60 alloys. (a,c) EBSD phase maps of the as-built and HT60 alloys. (b,d) ECC images of the as-built and HT60 alloys.

4. Discussion

4.1 Complex CB+SF network formation and the affected precipitation behavior

As illustrated above, the microstructure of the as-built Co25Cr5Mo5W alloy features a unique 3D complex SFs + CB networks within the near-pure γ-FCC matrix. We now first discuss the origin of forming such a distinctive defects configuration during LPBF, and then the unique precipitation behavior resulting from it.

In this study, the extremely high cooling rate during LPBF fully hinders the thermally-activated martensitic transformation, resulting in the near-pure γ-FCC matrix, agreeing with our previous findings [33]. However, we have to admit that the thermal cycles associated with high cooling rate also leads to the steady accumulation of thermal stresses hence uniform local strains throughout the matrix, which is confirmed by the high average geometrically necessary dislocation density in the as-built sample (see the kernel average misorientation map in Supplementary material Fig. S4a). Correspondingly in HT60 sample in Fig. S4b, the residual stress was slightly released due to sufficient thermal input. Such heavy local strains further drive the homogeneous nucleation of dislocation activities, including dislocation cross-slip and dissociation. The first term leads to the spontaneous formation the cell substructure when

associated with the flux and enrichment of certain solutes that show a strong solidification segregation tendency [34]. On the contrary the second term, which is much more pronounced for an alloy with low SFE, i.e., the CCM alloy here, triggers massive partial dislocation shearing events and results in the enhanced multi-directional SF nucleation alternative to the ε martensite growth, in the current metastable FCC phase. Hence, a dense complex CB+SF network is eventually constructed throughout the as-built sample. A schematic image showing the CB + SF network of the as-built sample can be found in supplementary Fig. S5.

Such complex CB+SF network strongly influences the precipitation behavior of the Laves phase during post heat treatment. Fig. 8a shows the typical as-built microstructure with only few black oxide particles embedded. At the initial 0 to 10 mins (Figs. 8b-c), precipitates selectively nucleate at the triple junctions of the CBs, followed by growing along the CBs. This observation suggests that the CBs are the preferred nucleation sites of the Laves precipitate, which can be understood in the following two aspects. Firstly, the segregation zone along CB provides a Laves-favorable chemical environment, i.e., relatively higher atomic level of Mo, W and Si than the cell interior, which lowers the nucleation barrier chemically for the Laves phase. Secondly, the high energy state of CB itself (bundles of dislocations) provides a high nucleation driving force, which is energetically needed for such a incoherent precipitate showing high interfacial energy with the matrix. In combination, CBs act as the preferential Laves nucleation sites and the dense distribution of the CBs finally leads to the locally heterogeneous yet overall near-homogeneous precipitation architecture. On the contrary, the dense SFs are not enriched in either Mo, W or Si hence not the prior Laves formation sites, contributing none to the Laves precipitation.

The STEM-EDS mappings of the precipitation microstructure of the HT7 sample are shown Fig. 8g, where Mo, W, Si segregate apparently along the CBs. Clearly, CBs can also serve as fast diffusion channels to transport the mass needed for the later growth and coarsening of the precipitates. This also explains why the triple junctions are the mostly favored by the Laves phase formation since the mass flow shall be the most sufficient there. After heat treatment for 15 mins, precipitates start to appear in the cell interior (see Fig. 8d), indicating the onset of homogeneous nucleation of the Laves phase. Further increasing the duration time allows a more even distribution of precipitates with sizes up to ~ 100 nm (see Figs. 8e and f).

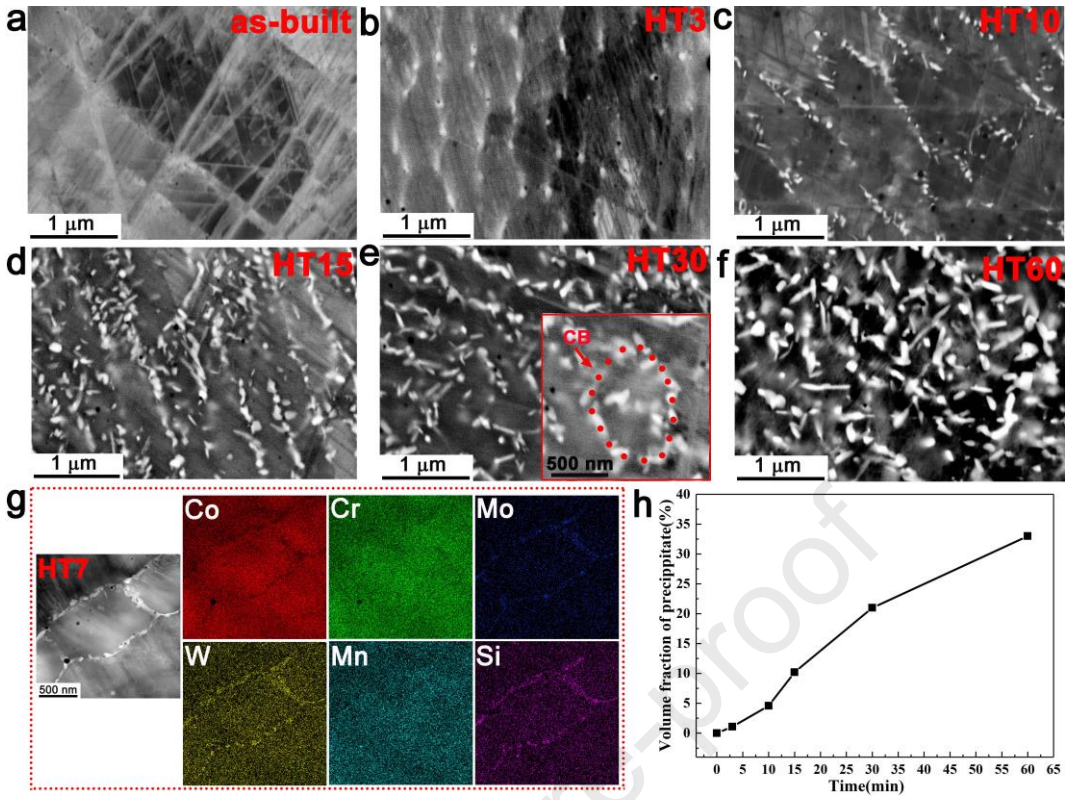

Fig. 8 (a-f) ECC images of the as-built, HT3, HT10, HT15, HT30 and HT60 samples, showing the precipitation course. (g) STEM-EDS mappings of the precipitation microstructure of the HT7 sample. (h) Plots of the volume fraction of precipitates against the duration time of heat treatment.

4.2 Deformation mechanisms of the as-built and heat-treated alloys

Owing to the different microstructure features, the as-built and heat-treated Co25Cr5Mo5W alloys exhibit distinct deformation behaviors. The TEM images (bright-filed (BF), dark-filed (DF) and HRTEM images) in Fig. 9 revealed the coexistence of γ phase, ε phase and deformation twins in ε phase in the as-built sample after tension. The DF images in Figs. 9b and c were taken by selecting diffraction spots of HCP matrix and twin in Fig. 9a, respectively, where the lamellas appearing bright are ε laths with a width of tens to hundreds of nanometers. Deformation twins can be observed within these ε laths, as shown in Fig. 9d. The angle between the basal planes of the matrix and twin is measured to be ~ 86°, indicating a $\{10\bar{1}2\}$ twin relationship. The orientation relationship between the FCC and HCP phases is: $\{111\}\gamma//(0001)\varepsilon$ and $<111>\gamma//<11\bar{2}0>\varepsilon$. These features are in accordance with the EBSD and ECC results in Fig. 7a-b, showing massive γ→ ε transformation during deformation. Such stress-induced phase transformation was also observed in the quasi-in-situ ECC experiment, in which the area scanned for ECC was precisely relocated after tensile testing to allow re-scanning at the exact same area, as shown

in Supplementary material Fig. S6. The 3D defects configuration constructed by SFs and CBs in the as-built alloy act as barriers for dislocation motion and also as nucleation sites for martensitic phase transformation. The stress-induced ε phase is different from the athermal martensite. The former is produced during deformation, while the latter is generated during the cooling process. The athermal martensite is reported to hinder dislocation motion, causing stress concentration at phase boundaries which will accelerate fracture [35]. In contrast, the stress-induced martensitic phase transformation has been widely used to improve the ductility, known as the transformation induced plasticity (TRIP) effect [36, 37]. The TRIP effect is more dominant in the as-built alloy when compared to the as-cast counterpart, where a large amount of athermal martensite already exists.

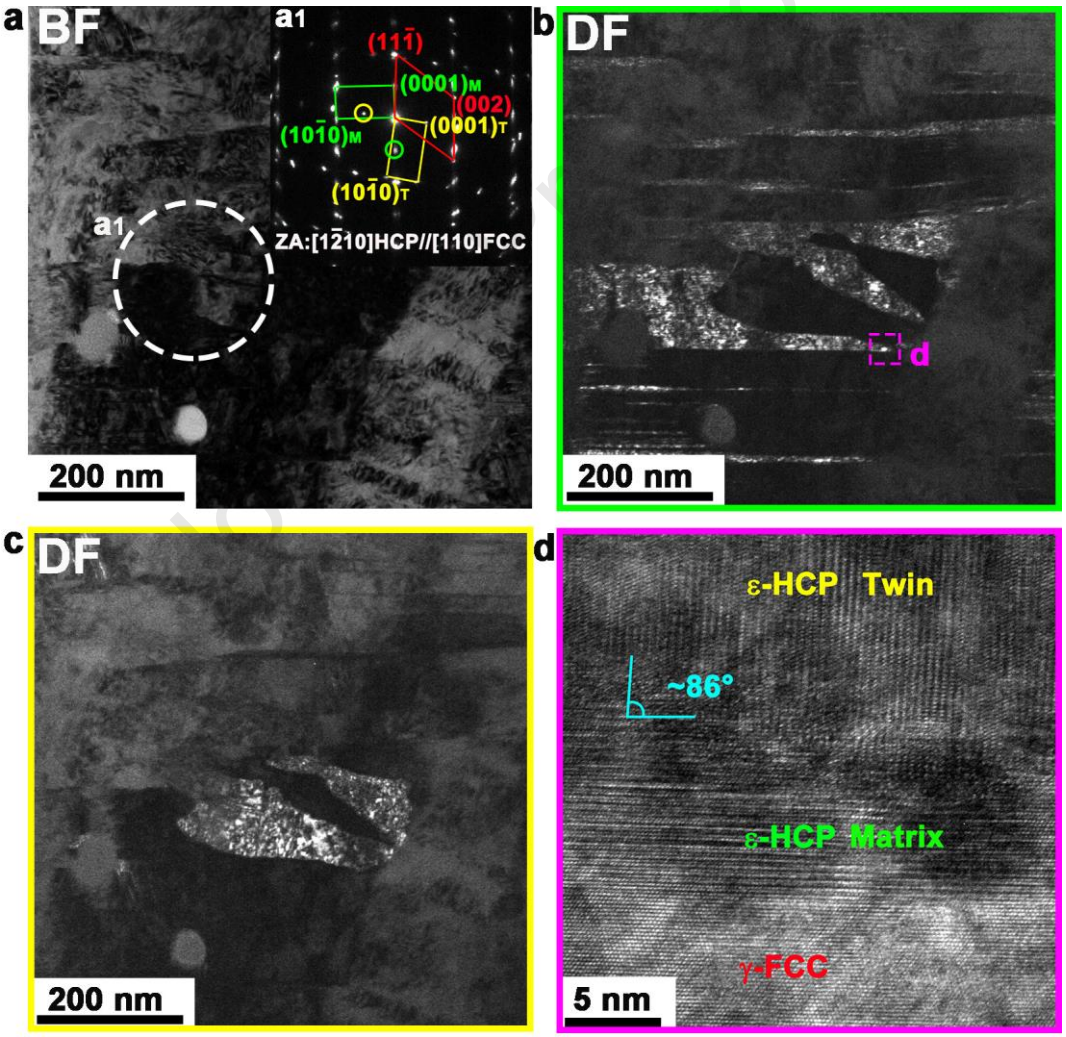

Fig. 9 (a) A bright field TEM image and its corresponding electron diffraction pattern of the as-built deformed sample. (b,c) The dark field TEM images by selecting diffraction spots of HCP matrix and twin for imaging. (d)A high resolution TEM image showing a deformation twin in the HCP phase.

Fig. 10 demonstrates the microstructure of the deformed HT60 alloy. Among precipitates, a vast number of SFs and/or thin ε laths with thickness of around several to tens of nanometers are presented in Fig. 10a, forming even denser weave structure (average spacing of ~ 300 nm) than the pre-existed SFs networks (~ 1.3 μm, as shown in Fig. 5f). It is likely because that, firstly, the evenly distributed Laves precipitates in the HT60 alloy provide additional contribution on, not only the nucleation but also the pinning of the further growth of the martensitic phase during deformation. And secondly, the overall occurrence of Laves precipitation changes the chemistry within the matrix, in particular lowers the atomic level of Mo, W and Si that reduces the stacking fault energy [38] and as a consequence, gives rise to the frequency of martensitic transformation during tension in the HT60 sample. Figs. 10a-d present examples showing the interaction between precipitates and stacking faults. Local stress fields exist between the precipitates and the γ matrix due to the differences in the lattice parameters of the precipitates and surrounding matrix. Once the tensile stress is applied, a large number of pre-existing SFs and newly-formed SFs can be activated and slip along the {111} planes to form parallel striations. The slip of the SFs is impeded by the precipitates, stretching the precipitates along the fault direction (Fig. 10b), and causing an increase in the yield strength and a loss in the ductility. This agrees well with the mechanical properties shown in Fig. 2a. Additionally, deformation twinning in the ε phase, mainly identified as the $\{10\bar{1}2\}$ type, is also found triggered in the deformed HT60 alloy, as shown in Figs. 10e and f. It occurs easily within the ε phase due to the small critical resolved shear stress, which is believed to well release the accumulated strain and coordinate plastic deformation.

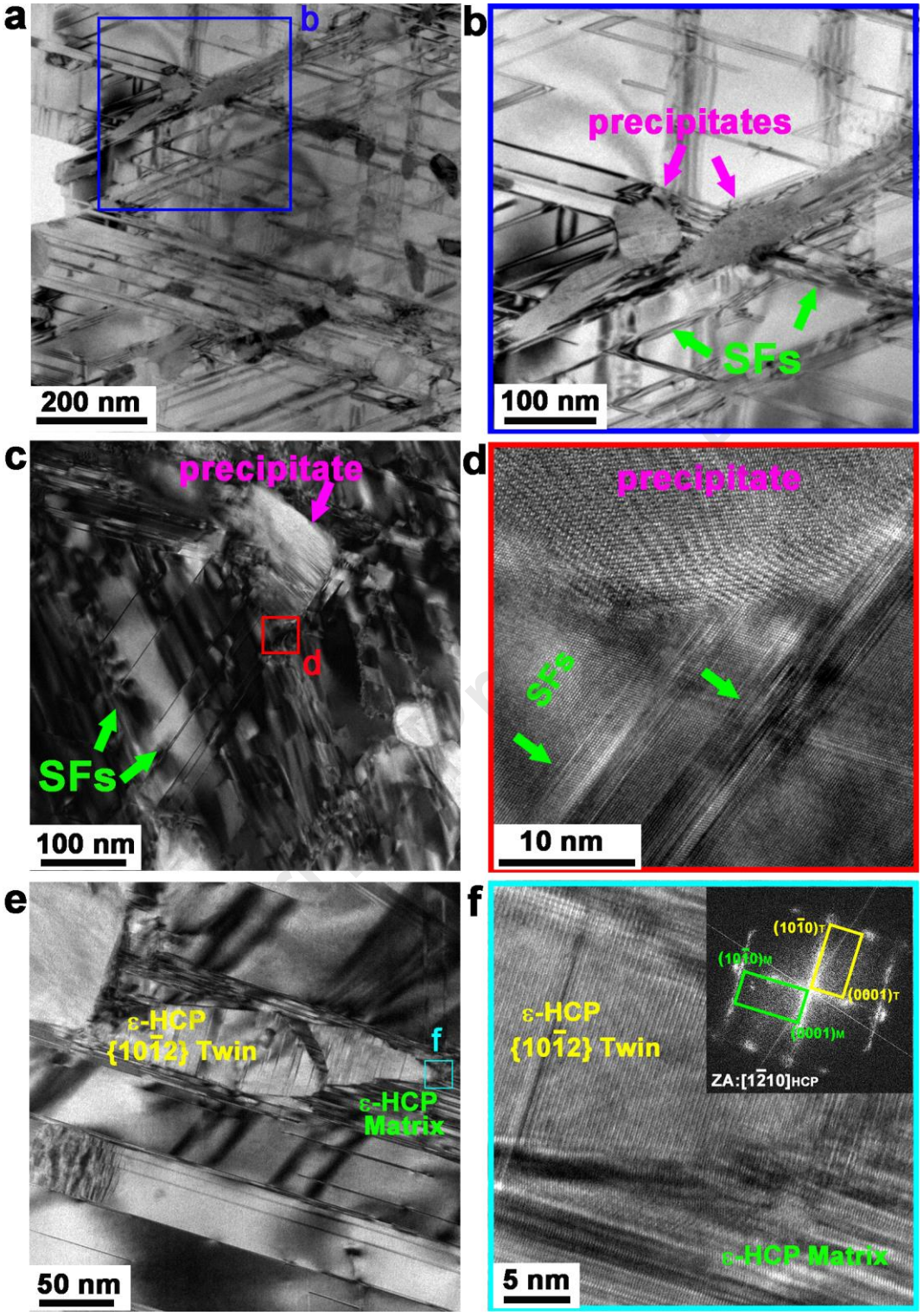

Fig. 10 (a-c) TEM BF images and (d) HRTEM image showing the widespread precipitates, SFs and their interactions in the deformed HT60 alloy. (e,f) TEM and high resolution TEM images showing the occurrence of deformation twinning in the HCP phase.

4.3 Origin of the two-stage strength-ductility performance

The strength-ductility trade-off behaves in two distinct stages upon heat treatment at 900 °C. The first stage is heat treatment within 15 mins, where the fast decrease in elongation presents without sufficient strength increment. The second stage is heat treatment beyond 15 mins, where the strength increases sharply but with less ductility sacrifice. In the following, we will discuss the origin of such two-stage strength-ductility performance by clarifying the strength contributions at each heat treatment condition, and evaluating the ductility loss in correspondence.

Generally, there are four strengthening mechanisms in polycrystalline materials: grain-boundary hardening (σ_G), solid-solution hardening (σ_{SS}), dislocation hardening (σ_D) and precipitation hardening (σ_P)[39, 40]. The following microstructure-relate model hence is used to evaluate the YS (σ_Y)[41],

$$\sigma_Y = \sigma_F + \sigma_G + \sigma_{SS} + \sigma_D + \sigma_P \quad (1)$$

where $\sigma_F = 165$MPa is applied as the lattice friction stress in our Co25Cr5Mo5W alloy[42].

For grain-boundary hardening, σ_G can be expressed by the classical Hall-Petch equation[18]:

$$\sigma_G = k_G \cdot d_G^{-\frac{1}{2}} \quad (2)$$

where k_G= 0.38 MPa·m$^{1/2}$ is the Hall-Petch coefficient [35], d_G is the average grain size. Here, we have to do two modifications considering the unique as-built microstructure features. First is the presence of dense SFs, which will generate additional resistance to dislocation motion in a similar Hall-Petch type. This gives an extra term in Eq. (3) and changes it to the following:

$$\sigma_G = k_G \cdot d_G^{-\frac{1}{2}} + k_{SF} \cdot t_{SF}^{-\frac{1}{2}} \quad (3)$$

where k_{SF} is the Hall-Petch coefficient for SFs, and we roughly assume k_{SF} equals to k_G according to [35] . t_{SF} is the average SF spacing. Since the SFs are thermally stable at high temperatures (no obvious changes upon 60 mins of heat treatment, see Fig. 5f), the t_{SF} value, ~1.3 μm, remains nearly unchanged across the investigated heat treatment states.

Second is the cell substructure, which is known to perform like typical high-angle GBs (although of low-angle nature) when encountering dislocations [43]. In this context, we simply substitute the grain size with the cell size d_λ [18, 43], which renews the above Eq. (4) as follows:

$$\sigma_G = k_G \cdot d_\lambda^{-\frac{1}{2}} + k_{SF} \cdot t_{SF}^{-\frac{1}{2}} \quad (4)$$

Where d_λ also keeps almost unchanged and is measured as 0.95 ± 0.05 μm from OM images. According to Eq. (5) and by inserting all the parameters listed in Table 2, the total σ_G is calculated as ~728 MPa.

Table 2. Parameters for calculating the strengthening contributions

Parameter	Value	Unit
CRSS,τ_{CRSS}	54	MPa [44]
Hall-Petch coefficient, k	0.38	MPa·m$^{1/2}$ [35]
Shear modulus, G	78.4	GPa [18]
Taylor factor, M	3.05	
Burgers vector, b	0.253	nm
Lattice constant, a	0.358	nm

For solid-solution hardening, the current LPBF Co25Cr5Mo5W alloys can be treated as a CoCr solvent matrix containing Mo, W, Mn, Si solutes, leading to a σ_{SS} expressed by[40]:

$$\sigma_{SS} = M \cdot \frac{G \cdot \varepsilon_S^{\frac{3}{2}} \cdot c^{\frac{1}{2}}}{700} \quad (5)$$

where$G$ is the shear modulus, c is the total molar ratio of Mo, W, Mn, Si elements solid-solutioned in the CoCr matrix phase. Following the instruction on the evaluation of ε_S given in ref. [18, 40], and considering the nearly unchanged c value (0.068),we evaluate σ_{SS} to be ~25 MPa for all the as-built and heat-treated alloys.

For dislocation hardening, we propose that most dislocations construct the CBs during thermal cycles, leaving low dislocation density in the cell interior (see Fig. 3 and 8), as also reported in other LPBF alloys [18, 20]. Therefore, to avoid repetition, we exclude the strengthening contribution from dislocations here.

For precipitation hardening, since the precipitates form only at CBs before 15 mins of heat treatment, the strengthening contribution from these precipitates reasonably overlays with that from the located CBs. In this perspective, we only consider those intragranular ones to be effective in precipitation hardening, beyond 15 mins of heat treatment, and evaluate σ_P by the classical Orowan mechanism due to the hard and unshearable nature of the dominating precipitates ($Co_3(Mo, W)_2Si$) [45-47]:

$$\sigma_P = \frac{0.538Gb\sqrt{f}}{D} \cdot \ln\left(\frac{D}{2b}\right) \quad (6)$$

Where G is the shear modulus, b is the Burgers vector of the matrix ($b = a/\sqrt{2}$ for FCC structure, where

a is lattice parameter), D is the real spatial diameter of precipitates (D=$\sqrt{3/2} \cdot d$, d is average diameter of the precipitates). By inserting the f (volume fraction, HT15 2.7 %, HT30 11.6 %, HT60 29.8 %) and d (mean diameter, HT15 90 ± 2 nm, HT30 100 ± 2 nm, HT60 101 ± 3 nm) data measured from over 5 different TEM images, the contribution from precipitation hardening of the HT15, HT30, and HT60 alloys are calculated as 83 MPa, 155 MPa, and 250 MPa, respectively.

Based on Eq. (1), we calculate the total (yield) strength of the as-built, HT3, HT7, HT10, HT15, HT30, and HT60 alloys as 913 MPa, 914 MPa, 915 MPa, 917 MPa, 997 MPa, 1070 MPa, and 1165 MPa, respectively, as plotted in Fig. 11. Apparently, these theoretically calculated values stay in reasonable error-scale with the experimental ones, suggesting that our understanding on the strength origins are fairly meaningful. This also sheds light on the understanding of the corresponding ductility performance. Before 15 mins of heat treatment, the heterogeneously formed Laves precipitates along CBs yield an inter-connected local stress concentration zone, which severely increases the stress level in the CB vicinity upon loading. Therefore, the cracks are easier to nucleate around the precipitates and the embedded high-stressed CBs further provide a crack propagation path and, as a consequence, deteriorate the overall ductility. Later after 15 mins of heat treatment, the newly formed in-grain precipitates distribute much more homogeneously, leading to a more uniform stress concentration level throughout the cell interior hence less impact on the ductility. We can now confidently summarize that the two-stage strength variation is mainly due to the change in precipitation hardening, and the turning point of mechanical properties at 15 mins heat treatment is because of the global start of the intragranular precipitation. It's interesting that a change in the elasticity modulus also appears at 15 mins heat treatment, which would also be closely related to the change in precipitation behaviors and will be further studied in the future.

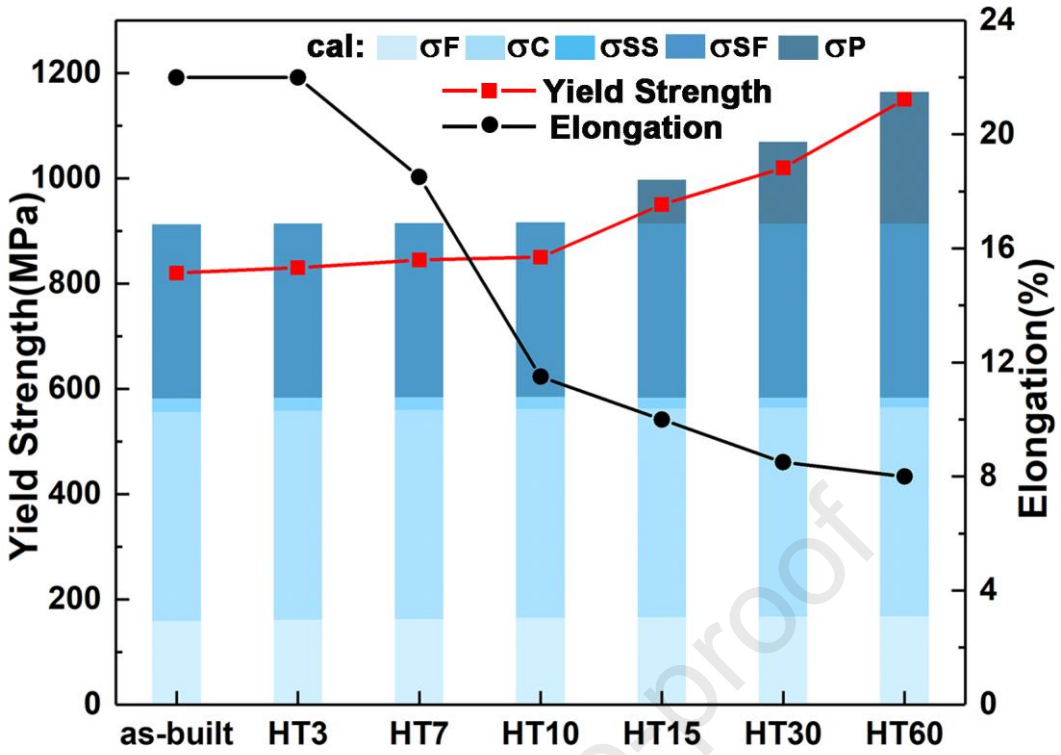

Fig. 11 Comparison between the calculated and experimentally obtained yield strength and elongation of the as-built, HT3, HT7, HT10, HT15, HT30, and HT60 alloys.

5. Conclusions

In this work, Co25Cr5Mo5W alloy has been fabricated by LPBF and heat treated at 900 °C for different periods. Based on mechanical properties, microstructure characterization and discussions, the results are summarized as following:

(1) By applying additive manufacturing, i.e., laser powder bed fusion technology, we successfully prepared a Co25Cr5Mo5W alloy with pure FCC structure, and realized a high strength-ductility combination via manipulating the precipitation behavior at 900 °C. The yield strength, ultimate tensile strength and elongation of the as-built and the HT60 samples are ~820 MPa, ~1185 MPa, ~22.3%, and ~1170 MPa,~1395 MPa, ~7.5 %, respectively.

(2) For the as-built alloy, the dense 3D networks constructed by cell boundaries and stacking faults offer a decent strengthening contribution, while the full ductile FCC matrix benefits the ductility.

(3) With 900 °C heat treatment, the strength-ductility variation behaves in two distinctive stages: the fast decrease in elongation without sufficient strength increment before 15 mins heat treatment, and the obvious increment in strength but with less ductility sacrifice after 15 mins heat treatment. Such two-stage strength-ductility variation is mainly due to the change in precipitation behaviors.

(4) The precipitates locate at CBs before 15 mins, whose pining effect against dislocations largely overlays with that of boundaries. Meanwhile, these CB particles generate near-continuous stress concentration along CBs, accelerating crack nucleation and propagation hence deteriorating the overall ductility. After 15 mins of heat treatment, intragranular precipitates appear. Their homogeneous distribution leads to not only an apparent increment in strength but also more uniform stress concentrations hence acceptable ductility loss.

Acknowledgments

We would like to thank the financial support from National Natural Science Foundation of China [grant number 52171130 (S.N.), 52101207 (J.H.)], Huxiang Youth Talents Support Program [grant number 2021RC3002 (S.N.)], the Science and Technology Innovation Program of Hunan Province [grant number 2022RC3035 (M.S.)] and Postgraduate Research Innovation Project of Central South University (2022ZZTS0399). ZBC would like to express his sincere thanks to the financial support from the Research Office and Research Institute of Advanced Manufacturing of the Hong Kong Polytechnic University [grant numbers P0039966 and P0041361]. YH is grateful for support from the Royal Society in the UK under Grant No. IEC\R3\193025. The Advanced Research Center of Central South University is sincerely appreciated for TEM and APT technical support.

Credit authorship contribution statement

Wenting Jiang: Conceptualization, Data Curation, Formal analysis, Writing - Original Draft, Review & Editing.

Xinglong An: Conceptualization, Data Curation, Formal analysis, Writing - Review &Editing.

Song Ni: Conceptualization, Formal analysis, Writing - Review &Editing, Supervision, Project

administration, Funding acquisition.

Li Wang: Data Curation,Formal analysis,Writing - Review &Editing.

Junyang He: Conceptualization, Data Curation,Writing - Review &Editing, Funding acquisition.

Zibin Chen: Formal analysis, Writing - Review &Editing.

Yi Huang: Formal analysis, Writing - Review &Editing.

Min Song: Formal analysis, Writing - Review & Editing, Project administration, Funding acquisition.

Data Availability

All data used during the study are available from the corresponding author by request.

Declaration of Competing Interest

The authors declare that they have no known competing financial interests or personal relationships that could have appeared to influence the work reported in this paper.

References

[1] J. Ni, H. Ling, S. Zhang, Z. Wang, Z. Peng, C. Benyshek, R. Zan, A.K. Miri, Z. Li, X. Zhang, J. Lee, K.J. Lee, H.J. Kim, P. Tebon, T. Hoffman, M.R. Dokmeci, N. Ashammakhi, X. Li, A. Khademhosseini, Three-dimensional printing of metals for biomedical applications, Mater. Today. Bio. 3 (2019) 100024.
[2] S. Bose, D. Ke, H. Sahasrabudhe, A. Bandyopadhyay, Additive manufacturing of biomaterials, Prog. Mater. Sci. 93 (2018) 45-111.
[3] D. Wei, A. Anniyaer, Y. Koizumi, K. Aoyagi, M. Nagasako, H. Kato, A. Chiba, On microstructural homogenization and mechanical properties optimization of biomedical Co-Cr-Mo alloy additively manufactured by using electron beam melting, Addit. Manuf. 28 (2019) 215-227.
[4] Z. He, N. Jia, H. Yan, Y. Shen, M. Zhu, X. Guan, X. Zhao, S. Jin, G. Sha, Y. Zhu, C.T. Liu, Multi-heterostructure and mechanical properties of N-doped FeMnCoCr high

entropy alloy, Int. J. Plast. 139 (2021)102965.
[5] C. Bonatti, D. Mohr, Large deformation response of additively-manufactured FCC metamaterials: From octet truss lattices towards continuous shell mesostructures, Int. J. Plast. 92 (2017) 122-147.
[6] Z. Wang, S.Y. Tang, S. Scudino, Y.P. Ivanov, R.T. Qu, D. Wang, C. Yang, W.W. Zhang, A.L. Greer, J. Eckert, K.G. Prashanth, Additive manufacturing of a martensitic Co–Cr–Mo alloy: Towards circumventing the strength–ductility trade-off, Addit. Manuf. 37 (2021) 101725.
[7] X. Dong, Y. Zhou, Q. Sun, Y. Qu, H. Shi, W. Liu, H. Peng, B. Zhang, S. Xu, J. Yan, N. Li, Fatigue behavior of biomedical Co–Cr–Mo–W alloy fabricated by selective laser melting, Mater. Sci. Eng. A 795 (2020) 140000.
[8] Y. Li, Y. Koizumi, A. Chiba, Dynamic recrystallization in biomedical Co-29Cr-6Mo-0.16N alloy with low stacking fault energy, Mater. Sci. Eng. A 668 (2016) 86-96.
[9] B. Wang, X. An, Z. Huang, M. Song, S. Ni, S. Liu, Nitrogen doped Co-Cr-Mo-W based alloys fabricated by selective laser melting with enhanced strength and good ductility, J. Alloy. Compd. 785 (2019) 305-311.
[10] K. Yamanaka, M. Mori, A. Chiba, Developing high strength and ductility in biomedical Co-Cr cast alloys by simultaneous doping with nitrogen and carbon, Acta Biomater. 31 (2016) 435-447.
[11] J. Wang, J. Zou, H. Yang, L. Zhang, Z. Liu, X. Dong, S. Ji, Exceptional strength-ductility synergy of additively manufactured CoCrNi medium-entropy alloy achieved by lattice defects in heterogeneous microstructures, J. Mater. Sci. Technol. 127 (2022) 61-70.
[12] D. Zhang, D. Qiu, M.A. Gibson, Y. Zheng, H.L. Fraser, D.H. StJohn, M.A. Easton, Additive manufacturing of ultrafine-grained high-strength titanium alloys, Nature 576(7785) (2019) 91-95.
[13] Y. Kajima, A. Takaichi, N. Kittikundecha, T. Nakamoto, T. Kimura, N. Nomura, A. Kawasaki, T. Hanawa, H. Takahashi, N. Wakabayashi, Effect of heat-treatment temperature on microstructures and mechanical properties of Co–Cr–Mo alloys fabricated by selective laser melting, Mater. Sci. Eng. A 726 (2018) 21-31.
[14] Y. Liu, Y. Yang, D. Wang, A study on the residual stress during selective laser melting (SLM) of metallic powder, Int. J. Adv. Manuf. Technol. 87(1-4) (2016) 647-656.
[15] W. Dong, X.A. Jimenez, A.C. To, Temperature-dependent modified inherent strain method for predicting residual stress and distortion of Ti6Al4V walls manufactured by wire-arc directed energy deposition, Addit. Manuf. 62 (2023) 103386.
[16] A.K. Syed, B. Ahmad, H. Guo, T. Machry, D. Eatock, J. Meyer, M.E. Fitzpatrick, X. Zhang, An experimental study of residual stress and direction-dependence of fatigue crack growth behaviour in as-built and stress-relieved selective-laser-melted Ti6Al4V, Mater. Sci. Eng. A 755 (2019) 246-257.
[17] L.H.M. Antunes, J.J. Hoyos, E.B. Fonseca, M. Béreš, P.F. da Silva Farina, E.S.N. Lopes, A.L. Jardini, R.M. Filho, Effect of phase transformation on ductility of

additively manufactured Co–28Cr–6Mo alloy: An in situ synchrotron X-ray diffraction study during mechanical testing, Mater. Sci. Eng. A 764 (2019) 138262.
[18] K. Li, Z. Wang, K. Song, K. Khanlari, X.-S. Yang, Q. Shi, X. Liu, X. Mao, Additive manufacturing of a Co-Cr-W alloy by selective laser melting: In-situ oxidation, precipitation and the corresponding strengthening effects, J. Mater. Sci. Technol. 125 (2022) 171-181.
[19] K. Ueki, M. Kasamatsu, K. Ueda, Y. Koizumi, D. Wei, A. Chiba, T. Narushima, Precipitation during γ-ε Phase Transformation in Biomedical Co-Cr-Mo Alloys Fabricated by Electron Beam Melting, Metals 10(1) (2020).
[20] M. Roudnická, O. Molnárová, J. Drahokoupil, J. Kubásek, J. Bigas, V. Šreibr, D. Paloušek, D. Vojtěch, Microstructural instability of L-PBF Co-28Cr-6Mo alloy at elevated temperatures, Addit. Manuf. 44 (2021) 102025.
[21] K. Li, J. Yang, Y. Yi, X. Liu, Y. Liu, L.-C. Zhang, W. Zhang, W. Li, D. Chen, S. Zhou, Enhanced strength-ductility synergy and mechanisms of heterostructured Ti6Al4V-Cu alloys produced by laser powder bed fusion, Acta Mater. 256 (2023) 119112.
[22] D. Wei, W. Gong, T. Tsuru, I. Lobzenko, X. Li, S. Harjo, T. Kawasaki, H.-S. Do, J.W. Bae, C. Wagner, G. Laplanche, Y. Koizumi, H. Adachi, K. Aoyagi, A. Chiba, B.-J. Lee, H.S. Kim, H. Kato, Si-addition contributes to overcoming the strength-ductility trade-off in high-entropy alloys, Int. J. Plast. 159 (2022) 103443.
[23] M. Zhang, Y. Yang, C. Song, Y. Bai, Z. Xiao, An investigation into the aging behavior of CoCrMo alloys fabricated by selective laser melting, J. Alloy. Compd. 750 (2018) 878-886.
[24] M. Roudnická, J. Kubásek, L. Pantělejev, O. Molnárová, J. Bigas, J. Drahokoupil, D. Paloušek, D. Vojtěch, Heat treatment of laser powder-bed-fused Co – 28Cr – 6Mo alloy to remove its microstructural instability by massive FCC→HCP transformation, Addit. Manuf. 47 (2021) 102265.
[25] Z. Ye, C. Li, Z. Huang, H. Luo, F. Chen, Z. Yan, J. Li, C. Xu, Z. Zhang, The effect of solution and aging treatments on the microstructure and mechanical properties of a selective laser melted CoCrMo alloy, J. Mater. Sci. 57(11) (2022) 6445-6459.
[26] E. Santecchia, A. Gatto, E. Bassoli, L. Denti, B. Rutkowski, P. Mengucci, G. Barucca, Precipitates formation and evolution in a Co-based alloy produced by powder bed fusion, J. Alloy. Compd. 797 (2019) 652-658.
[27] W. Wei, Y. Zhou, Q. Sun, N. Li, J. Yan, H. Li, W. Liu, C. Huang, Microstructures and Mechanical Properties of Dental Co-Cr-Mo-W Alloys Fabricated by Selective Laser Melting at Different Subsequent Heat Treatment Temperatures, Metallurgical and Materials Transactions A 51(6) (2020) 3205-3214.
[28] W. Wei, Y. Zhou, W. Liu, N. Li, J. Yan, H. Li, Microstructural Characterization, Mechanical Properties, and Corrosion Resistance of Dental Co-Cr-Mo-W Alloys Manufactured by Selective Laser Melting, J. Mater. Eng. Perform. 27(10) (2018) 5312-5320.
[29] Y. Kajima, A. Takaichi, T. Nakamoto, T. Kimura, Y. Yogo, M. Ashida, H. Doi, N.

Nomura, H. Takahashi, T. Hanawa, N. Wakabayashi, Fatigue strength of Co-Cr-Mo alloy clasps prepared by selective laser melting, J. Mech. Behav. Biomed. Mater. 59 (2016) 446-458.
[30] Y. Lu, S. Wu, Y. Gan, S. Zhang, S. Guo, J. Lin, J. Lin, Microstructure, mechanical property and metal release of As-SLM CoCrW alloy under different solution treatment conditions, J. Mech. Behav. Biomed. Mater. 55 (2015) 179-190.
[31] P. Mengucci, G. Barucca, A. Gatto, E. Bassoli, L. Denti, F. Fiori, E. Girardin, P. Bastianoni, B. Rutkowski, A. Czyrska-Filemonowicz, Effects of thermal treatments on microstructure and mechanical properties of a Co-Cr-Mo-W biomedical alloy produced by laser sintering, J. Mech. Behav. Biomed. Mater. 60 (2016) 106-117.
[32] Y. Zhou, Q. Sun, X. Dong, N. Li, Z.J. Shen, Y. Zhong, M. Eriksson, J. Yan, S. Xu, C. Xin, Microstructure evolution and mechanical properties improvement of selective laser melted Co-Cr biomedical alloys during subsequent heat treatments, J. Alloy. Compd. 840 (2020) 155664.
[33] W. Jiang, X. An, W. Liu, S. Ni, M. Song, Microstructure and hardness of solution treated and cold-rolled Co75Cr25 alloy, Mater. Charact. 181 (2021) 111521.
[34] K.G. Prashanth, J. Eckert, Formation of metastable cellular microstructures in selective laser melted alloys, J. Alloy. Compd. 707 (2017) 27-34.
[35] M. Mori, K. Yamanaka, S. Sato, S. Tsubaki, K. Satoh, M. Kumagai, M. Imafuku, T. Shobu, A. Chiba, Strengthening of biomedical Ni-free Co-Cr-Mo alloy by multipass "low-strain-per-pass" thermomechanical processing, Acta Biomater. 28 (2015) 215-224.
[36] N.C. Ferreri, R. Pokharel, V. Livescu, D.W. Brown, M. Knezevic, J.-S. Park, M.A. Torrez, G.T. Gray, Effects of heat treatment and build orientation on the evolution of ϵ and α' martensite and strength during compressive loading of additively manufactured 304L stainless steel, Acta Mater. 195 (2020) 59-70.
[37] Z. Li, S. Zhao, R.O. Ritchie, M.A. Meyers, Mechanical properties of high-entropy alloys with emphasis on face-centered cubic alloys, Prog. Mater. Sci. 102 (2019) 296-345.
[38] K. Jeong, J.-E. Jin, Y.-S. Jung, S. Kang, Y.-K. Lee, The effects of Si on the mechanical twinning and strain hardening of Fe–18Mn–0.6C twinning-induced plasticity steel, Acta Mater. 61(9) (2013) 3399-3410.
[39] F. An, J. Hou, J. Liu, B. Qian, W. Lu, Deformable κ phase induced deformation twins in a CoNiV medium entropy alloy, Int. J. Plast. 160 (2023) 103509.
[40] J.Y. He, H. Wang, H.L. Huang, X.D. Xu, M.W. Chen, Y. Wu, X.J. Liu, T.G. Nieh, K. An, Z.P. Lu, A precipitation-hardened high-entropy alloy with outstanding tensile properties, Acta Mater. 102 (2016) 187-196.
[41] N. Kamikawa, K. Sato, G. Miyamoto, M. Murayama, N. Sekido, K. Tsuzaki, T. Furuhara, Stress–strain behavior of ferrite and bainite with nano-precipitation in low carbon steels, Acta Mater. 83 (2015) 383-396.
[42] K. Yamanaka, M. Mori, S. Sato, A. Chiba, Stacking-fault strengthening of biomedical Co-Cr-Mo alloy via multipass thermomechanical processing, Sci. Rep. 7(1) (2017) 10808.

[43] H. Duan, B. Liu, A. Fu, J. He, T. Yang, C.T. Liu, Y. Liu, Segregation enabled outstanding combination of mechanical and corrosion properties in a FeCrNi medium entropy alloy manufactured by selective laser melting, J. Mater. Sci. Technol. 99 (2022) 207-214.
[44] Koji Hagihara, Takayoshi Nakano, K. Sasaki, Anomalous strengthening behavior of Co–Cr–Mo alloy single crystals for biomedical applications, Scr. Mater. (123) (2016) 149-153.
[45] B. Kim, E. Boucard, T. Sourmail, D. San Martín, N. Gey, P.E.J. Rivera-Díaz-del-Castillo, The influence of silicon in tempered martensite: Understanding the microstructure–properties relationship in 0.5–0.6wt.% C steels, Acta Mater. 68 (2014) 169-178.
[46] Z. Wang, I. Baker, W. Guo, J.D. Poplawsky, The effect of carbon on the microstructures, mechanical properties, and deformation mechanisms of thermo-mechanically treated Fe40.4Ni11.3Mn34.8Al7.5Cr6 high entropy alloys, Acta Mater. 126 (2017) 346-360.
[47] T. Gladman, Precipitation hardening in metals, Mater. Sci. Technol. 15(1) (2013) 30-36.

Credit authorship contribution statement

Wenting Jiang: Conceptualization, Data Curation, Formal analysis, Writing - Original Draft, Review & Editing.

Xinglong An: Conceptualization, Data Curation, Formal analysis, Writing - Review &Editing.

Song Ni: Conceptualization, Formal analysis, Writing - Review &Editing, Supervision, Project administration, Funding acquisition.

Li Wang: Data Curation,Formal analysis,Writing - Review &Editing.

Junyang He: Conceptualization, Data Curation,Writing - Review &Editing, Funding acquisition.

Zibin Chen: Formal analysis, Writing - Review &Editing.

Yi Huang: Formal analysis, Writing - Review &Editing.

Min Song: Formal analysis, Writing - Review & Editing, Project administration, Funding acquisition.

Declaration of interests

☒ The authors declare that they have no known competing financial interests or personal relationships that could have appeared to influence the work reported in this paper.

☐ The authors declare the following financial interests/personal relationships which may be considered as potential competing interests: